surfaces

MDPI

Review

Catalytically Active Materials Visualized by Scanning Photoelectron Spectro-Microscopy

Matteo Amati [1], Lada V. Yashina [2,3], Philipp Winkler [4], Kevin Sparwasser [5,†], Zygmunt Milosz [1], Günther Rupprechter [4] and Luca Gregoratti [1,*]

[1] Elettra-Sincrotrone Trieste S.C.p.A., SS14-Km163.5 in Area Science Park, 34149 Trieste, Italy
[2] Lomonosov Moscow State University, Leninskie Gory 1 Bld. 3, 119991 Moscow, Russia
[3] N.N. Semenov Federal Research Center for Chemical Physics, Kosygina Street 4, 119991 Moscow, Russia
[4] Institute of Materials Chemistry, TU Wien, Getreidemarkt 9, 1060 Vienna, Austria; guenther.rupprechter@tuwien.ac.at (G.R.)
[5] Max-Planck-Institut für Eisenforschung GmbH, Microstructure Physics and Alloy Design, 40237 Düsseldorf, Germany; kevin.sparwasser@statpeel.com
* Correspondence: luca.gregoratti@elettra.eu; Tel.: +39-0403758025
† Current address: Stat Peel Ltd., 8750 Glarus, Switzerland.

Abstract: Modern catalysts are complex systems whose performance depends both on space and time domains and, most importantly, on the operational environment. As a direct consequence, understanding their functionalities requires sophisticated techniques and tools for measurement and simulation, addressing the proper spatial and temporal scale and being capable of mimicking the working conditions of every single component, such as catalyst supports, electrodes, electrolytes, as well as of the entire assembly, e.g., in the case of fuel cells or batteries. Scanning photoelectron spectro-microscopy (SPEM) is one of the approaches that allow combining X-ray photoelectron spectroscopy with sub-micron spatial resolution; in particular, the SPEM hosted at the ESCA Microscopy beamline at Elettra has been upgraded to conduct in situ and operando experiments. Three different case studies are presented to illustrate the capabilities of the SPEM in the investigation of catalytic materials in different conditions and processes.

Keywords: heterogeneous catalysis; scanning photoemission microscopy; XPS; ORR; metal particles

Citation: Amati, M.; Yashina, L.V.; Winkler, P.; Sparwasser, K.; Milosz, Z.; Rupprechter, G.; Gregoratti, L. Catalytically Active Materials Visualized by Scanning Photoelectron Spectro-Microscopy. *Surfaces* **2024**, *7*, 442–459. https://doi.org/10.3390/surfaces7030028

Academic Editor: Nicolas Alonso-Vante

Received: 11 April 2024
Revised: 20 June 2024
Accepted: 22 June 2024
Published: 26 June 2024

1. Introduction

Materials for catalysis are a key component in the chemical industry, oil, fuel, and energy production chains, and new energy harvesting technologies, to name only the most important fields. Research is continuously looking for new materials with improved and tailored performance and strives to satisfy the continuously tightened environmental regulations. Modern catalysts are complex systems whose performances depend on both space and time domains and, most importantly, on the operational environment [1,2]. As a direct consequence, a deep understanding of their functionalities necessitates sophisticated techniques and tools for measurement and simulation capable of providing information at the proper spatial and temporal scale and capable of mimicking the working conditions of systems and their components, such as the catalyst supports, electrodes, electrolytes, as well as of the entire assembly such as in the case of fuel cells or batteries. To satisfy this statement, the complementary capabilities of synchrotron-based microscopy methods in terms of imaging, spectroscopy, spatial resolution, and variable probing depths have opened unique and wide opportunities to explore the structure and chemical composition of morphologically complex catalytic systems at proper length and time scales and correlate them to the fabrication or operating conditions [3–6].

Most of the processes involved in heterogeneous catalysis occur at the catalyst surface, chemically and surface-sensitive techniques are thus highly required for their investigation [7]; among them, X-ray photoelectron spectroscopy (XPS) has been widely used to

characterize catalytic systems with its probing depth limited to the few topmost atomic layers of the probed surfaces. XPS provides information on the elemental and chemical composition of surfaces and, to some extent, interfaces even in the case of complex materials where, for instance, functional groups or adsorbates are present and may interact with sub-surface layers modifying the local chemical and electronic environment. Despite XPS having been developed as a purely spectroscopic technique, it became clear about 40 years ago that the possibility of spatially resolved measurements is fundamental to overcoming the materials gap, which is ubiquitous in materials development; the scanning photoelectron microscope (SPEM) is one of the approaches that allowed combining XPS with sub-micron spatial resolution [8].

The first SPEM microscopes were developed in the 1990s exploiting the features of the revolutionary 3rd generation synchrotron light sources built in Grenoble (ESRF) and Berkely (ALS) and later in many other countries and the improved lithographic processes for the production of Fresnel lenses such as zone plates (ZP) [9]. The ZP-based SPEM design, suitable in particular for core-level imaging and spectroscopy, implemented in the first end stations immediately showed the capability of such instruments to achieve sub-micrometer spatial resolutions while keeping a good energy resolution mandatory for XPS spectroscopy. Over the decades, other focusing systems based on mirrors or refractive lenses have been designed and implemented in other SPEMs to allow spatially resolved angular photoemission (ARPES), low photon energy science, and other technical approaches. The installation and diffusion of X-ray photoelectron emission microscopes (PEEMs) [10], a full-field spectro-microscopy approach for spatially resolved XPS, in synchrotron laboratory as an alternative approach particularly suitable for dynamic studies, pushed SPEM technology to improve the lateral resolution which is intrinsically better in XPEEMs. Modern SPEMs are characterized by sub-100 nm spatial resolutions allowing a large variety of materials characterization while current PEEMs may achieve spatial resolutions of 20–30 nm or even better. Assuming the X-ray spot generated by a ZP has a Gaussian line shape, one of the best parameters to characterize the spatial resolution is to compare the full-width half maximum (FWHM) of the focused X-ray spot. The best documented SPEM X-ray spot FWHM has been obtained at Spring8 providing a FWHM of 70 nm [11]. The energy resolution is the other fundamental parameter to be considered for XPS measurements; it strongly depends on the X-ray monochromaticity, sample temperature, the characteristics of the electron analyzer, etc.; current SPEMs designed for core level analysis in the soft X-ray range, like the one at the ESCA Microscopy beamline at Elettra, can operate at <200 meV overall energy resolution while those specializing in low energy ARPES can do it at tens of mV or lower [12].

Depending on the desired features, modern SPEMs may use other focusing elements such as mirrors or refractive lenses, the performance of which is continuously improving.

To fulfill the increasing demand for in situ and operando sample environments, modern SPEMs exploit some of their distinctive flexibilities if compared to PEEMs, such as the independence of spatial resolution from sample morphology, the adaptability to complex sample setups, and many others. One of the most important recent improvements in SPEM design is the possibility to operate SPEMs at near ambient pressures. Following the development of XPS spectroscopes capable of analyzing samples at pressures as high as tens or hundreds of mbar, which occurred at the beginning of this century, only a few years ago the first SPEM microscope able to operate at pressures up to 1 mbar was opened to the users' communities [13].

The SPEM hosted at the ESCA Microscopy beamline at Elettra, in particular, was designed in 1980 and started its service to the user community in 1984; since then, it has been upgraded several times, increasing its capacity to conduct in situ and operando experiments, which are also essential for the investigation of catalytic processes, especially when applied to complex systems such as batteries, capacitors, or fuel cells. Understanding surface–interfacial systems requires, in fact, essential knowledge of details such as the atomic arrangements, compositional and chemical profiles, and, more importantly, their

response to external stimuli such as temperature, electric and magnetic fields, or light and gas exposure. In the modern scientific debate, all these external conditions are condensed in the so-called "sample environment". Modern SPEMs can provide customizable sample environments and very few limitations in sample geometry and surface morphology while keeping imaging and nano-spot spectroscopy at adequate energy and lateral resolutions [14,15].

This manuscript will focus on illustrating the capabilities of the SPEM at Elettra in the investigation of catalytic materials in different conditions and processes; a first example will report on oxygen reduction reactions (ORR) on electrochemical cells to study the electrochemical properties of graphene. In the second example, the size and support effects of catalytically active metal particles will be addressed by correlative application of two microscopy techniques; Rh particles on different substrates have been used to study the inactive and active states in the H_2 oxidation reaction. In the last contribution, an example of correlative microscopy for nanoscale exploration of structure–function relationships in catalytic materials is presented.

2. Materials and Methods

The SPEM hosted at the ESCA Microscopy beamline at the Elettra synchrotron light source uses a direct approach to add the spatial resolution to photoemission and to chemically characterize surfaces at the submicron scale, i.e., the uses a small, focused X-ray photon probe to illuminate the sample. Samples can be raster scanned with respect to the microprobe to generate chemical maps of specific elements or to acquire XPS spectra from specific points [16,17].

To produce a sub-micrometric beam spot, the incoming X-ray beam is focused by means of a lithographically made Fresnel Zone Plates (ZP) [18]. In the SPEM, only the first diffraction order is selected and the higher ones are blocked by an additional pinhole, the Order Selecting Aperture (OSA), while the straight radiation passing through the ZP (the zeroth order), is stopped by a metallic X-ray absorbing layer lithographically grown on the ZP center (central stopper). With a typical optical set-up, 200–250 μm diameter, 50–100 nm outermost ring, 80 μm central stopper ZP, 75 μm wide OSA, and photon energy in the 400–1200 eV range, a photon beam down to a spot of 130–180 nm diameter and 5–15 mm focal length can be achieved [16,17]. Both the spot dimension and focal length are a function of the photon energy.

Samples are placed in the focal point of the optics, and then raster scanned in the plane normal to the beam by two sets of motors: (i) stepper motors for large millimeter-wide movements and a minimum step of 1 μm, and (ii) a piezoelectric stage with a 100 × 100 μm scanning range, and a minimum step movement of 5 nm for high spatial resolution imaging of samples.

Due to the short focal length, the Hemispheric Electron Analyzer (HEA), used to detect the photoelectrons, has to be placed at 30° with respect to the sample surface. This configuration strongly enhances the surface sensitivity of the instrument. The HEA equips a delay line electron detector that is binned to 48 channels [19].

The SPEM can be operated in two modes: (i) imaging spectro-microscopy and (ii) micro-spot spectroscopy. In the imaging mode, the spatial distribution of the elements, or their chemical states, is recorded by collecting photoelectrons within a selected kinetic energy window while scanning the specimen with respect to the microprobe, creating so-called chemical maps with a submicron spatial resolution. In micro-spot mode, the setup is identical to a conventional XPS system, but spectra are measured from selected submicron spots on the sample. The overall energy resolution is better than 200 meV [16,17].

3. Results

3.1. Oxygen-Containing Functional Groups on Carbon Electrodes and ORR Processes

The oxygen reduction reaction (ORR) is a key process that governs the operation of fuel cells [20] and metal/air batteries, which grants, to date, the highest specific energy

among energy storage devices [21–23]. It is known that ORR proceeds on carbon surfaces in the absence of a catalyst, with electrochemical activity being determined by microstructure, composition, and defects on carbon surfaces [24]. The idea that various graphene imperfections (vacancies, impurity atoms, and corresponding functional groups) may catalyze ORR has been under broad discussion during the last decades [25–29]. Among different imperfections, oxygen-containing functional groups are of interest since they are unavoidably present on the surface of carbon materials [30–33]. Oxygen functional groups, almost unavoidably existing on the graphene surface, can serve as adsorption sites for ORR intermediates. Moreover, some oxygen-containing functionalities provide an increase in the density of electronic states (DOS) near the Fermi level (FL). Both factors are positive towards the electron transfer rate. The negative factor is that any oxygen-containing groups induce bandgap opening. Its width depends on oxygen content; ultimately, oxygenation results in a fully insulating material. Therefore, oxygen concentration should be optimized [34,35].

To explore the influence of O-groups on the aprotic ORR, we used a model carbon electrode–graphene. Aprotic ORR is now under particular interest due to the development of aprotic metal–air batteries. We used a model electrochemical cell [36]. To uncover the role of oxygen groups in aprotic ORR, model carbon electrodes possessing a certain number of functional groups and other defects are required. Moreover, the flat morphology of graphene is convenient for model electrochemical research. The type and composition of defects arising after oxygenation were studied by XPS. The spectral observations were performed in operando conditions during the discharge of an electrochemical cell, with a solid electrolyte being used for this purpose [36].

In our experiments, we used commercial graphene. It presents large-scale graphene on copper foil, possessing typically seldom bilayer islands randomly distributed over the surface; the corresponding mean density is about $3 \cdot 10^6$ cm^{-2} in our case. The graphene was transferred onto the solid electrolyte. First, scanning X-ray photoemission microscopy revealed that atomic oxygen induces graphene oxidation. This oxidation is not uniform. We observed the formation of certain structures. In detail, relatively mobile epoxy groups uniformly cover single-layer graphene, but their concentration is essentially lower for bilayer islands [37]. Carbonyl and lactones are located exclusively at the centers of the islands. Such oxidation behavior can be understood from the fact that the centers of the bilayer islands are rather defective and undergo faster and deeper oxygen attacks. Spatially resolved data are collected in Figure 1. As it follows from the C *1s* spectrum in Figure 1a, at the beginning epoxy groups are present solely at the surface of oxidized graphene on Cu foil. Both maps C *1s* and O *1s* in Figure 1 demonstrate a uniform distribution of epoxy groups in areas of single-layer graphene. This correlates with Raman maps in Figure 1m,n. The strongly increased D-mode is related to oxidation and revealed both for the initially defect-free single-layer regions and the initially very defective centers of bilayer regions (see the spectra in Figure 1o). Correspondingly, in the O *1s* map in Figure 1f, elemental contrast arises, which pinpoints less intensive oxidation of bilayer regions and a minor D-mode. The fact that bilayer regions possess lower reactivity was discussed earlier and explained by the higher stability of bilayer graphene, etc. We highlight the decisive role of substrate with respect to epoxy group stability in graphene. After a certain exposure, elemental maps exhibit stronger contrast due to the non-uniform distribution of oxygen-containing species. The O *1s* maps in Figure 1f–h show three different intensity levels. Bright 1 μm spots are randomly positioned in the large medium-intensity areas, which are composed of single-layer graphene. It is uniformly covered by epoxy groups. These high-intensity areas reveal that the centers of bi-layer areas are the most oxidized regions. They comprise solely one layer and should be quite defective. Inverted contrast is naturally revealed in the C *1s* maps in Figure 1j–l. Moreover, the distribution of oxygen-containing carbon species directly corresponds to the maps of oxygen intensity distribution. In contrast to the previously reported thermal oxidation of Cu-supported graphene, when copper is oxidizing in the areas near defected places of graphene, we found exclusive oxidation of graphene rather than copper underneath, which remains intact according to Cu *3p* spectra. We suppose

that although epoxy species are uniformly distributed, carbonyl and lactone species are positioned preferentially in the centers of bilayer islands. This assumption is in line with Raman maps and spectra in Figure 1m–o. The G/D intensity ratio for the centers of bilayer islands is similar for single-layer graphene, however, the nature of defects is different. Spectral peaks for centers are essentially broader due to the high defect concentration in the original graphene.

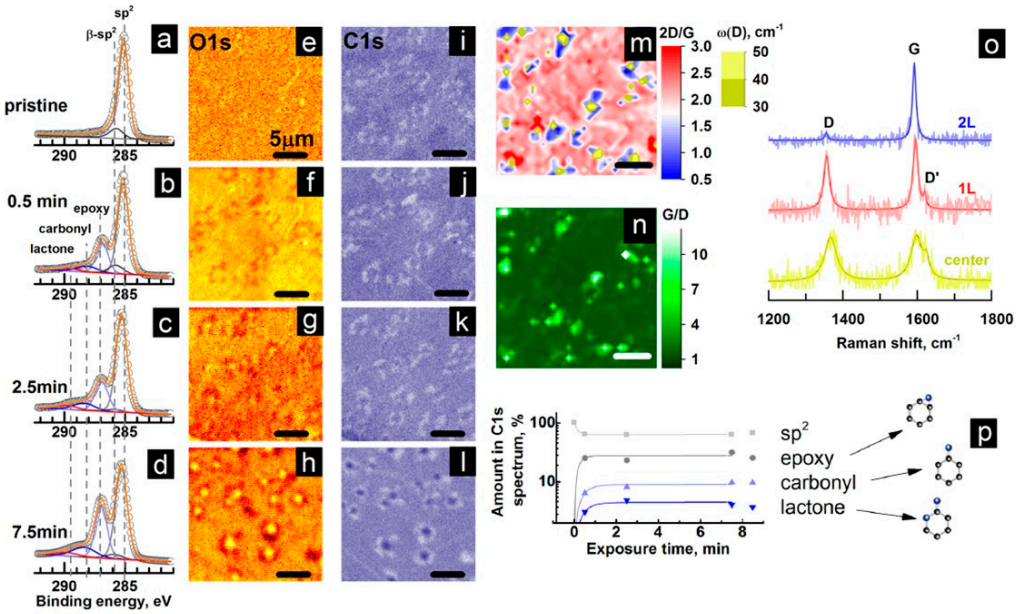

Figure 1. Evolution of the surface composition upon atomic oxygen treatment of graphene on Cu foil: C *1s* spectra (**a**–**d**), O *1s* (**e**–**h**), and C *1s* (**i**–**l**) maps. Typical Raman 2D/G band intensity ratio (in red/blue) and D (in yellow/mustard) width (**m**) and G/D map (**n**) of the sample oxidized for 7.5 min and representative Raman spectra for single layer areas, two-layer regions, and their central parts (**o**). Variation of the relative intensity of the C *1s* spectral features (**p**). The scale bar corresponds to 5 μm for all maps [37]. Reprinted with permission from [37]. Copyright 2017 American Chemical Society.

In aprotic media, oxygen is reduced through a one-electron reaction [38]:

$$O_2 + e^- = O_2^-. \qquad k_1 \qquad (1)$$

Modern interest is related to aprotic ORR in the presence of metal ions with respect to different aprotic metal–oxygen batteries (Li, Na, Mg, etc.). In this case, the ORR products are typically metal superoxides, peroxides, or oxides, due to the strong coupling of the metal ion with superoxide species. Peroxides can be formed for Li-O_2 cells as a result of second electron transfer:

$$O_2^- + e^- + 2Li^+ = Li_2O_2, \qquad k_2 \qquad (2)$$

and due to superoxide disproportionation as well.

Moreover, graphene degradation under the attack of LiO_2 is observed

$$3/2\ O_2^- + C = CO_3^{2-} \qquad k_{deg} \qquad (3)$$

We have measured k_1 electrochemically and found that the k_1 value for graphene shows no obvious trend upon the oxidation degree [23]. In contrast to our expectations, there is no noticeable catalytic effect of oxygen groups (epoxy, carbonyl, and lactone groups) for one-electron ORR in aprotic media. We also evaluated the rate constants k_2 of the reaction (2) and k_{deg} (3). At the same time, k_2 indeed depends on O-groups amount; the corresponding rate constant increases for higher oxygen concentration to 16 at.%. At

the same time, not only k_2 but also k_{deg} depends on the oxidation degree. Therefore, oxygen-containing groups promote carbon oxidation by LiO_2.

To obtain further insight into the influence of oxygen-containing groups on the graphene degradation by attack of superoxide species we have carried out model photoemission experiments [23]. The direct spectral observations were performed using operando XPS of the discharge. Here, we used a model Li-O_2 electrochemical cell with a Li^+-conductive solid electrolyte [36,39]. The cell is schematically presented in Figure 2c. Bilayer graphene coverage was prepared by two sequential transfers to solid electrolyte membranes. Graphene was oxidized by UV treatment in the O_2 atmosphere in this case. The pristine graphene sample was transferred to the preparation chamber and cleaned by degassing in UHV at 80 °C and heating at 190 °C. The cell was assembled in an Ar-filled glove pack and moved in the analytical chamber of the spectrometer without air exposure. The cell was discharged galvanostatically under 0.1 mbar of O_2 inside the near ambient pressure XPS chamber. In the course of the experiment, C *1s*, O *1s*, and Li *1s* spectra were acquired. The enhanced lithium and oxygen signals evidence the formation of discharge products. In C *1s* spectra, oxidation is revealed by the appearance of two additional components. The component at 6.0–6.5 eV higher binding energy relative to the graphene is due to carbonate. The second new component is shifted by 2–2.5 eV, which is slightly more than expected for -COLi groups (0.9–1.2 eV). Therefore, we assign this component to the ether-like group in organic (or semi-organic) carbonates -**C**-O-C(=O)O having a chemical shift of 1.8–2.2 eV. The minor shift (ca. +0.5 eV) of binding energy for all components can be referred to as the work function variation during discharge, or by the clustering of oxygen-containing groups at the higher oxidation level.

We have compared the fraction of different spectral components in C *1s* spectra related to oxidized and pristine graphene electrodes at the same depth of discharge. The latter was estimated from XP-spectra using the Li-to-C atomic ratio. The spectra reveal the higher degradation rate for originally oxidized graphene since more carbonate and ether-like species are formed in this case. It was also found that the fraction of carbonate and ether components grow simultaneously, which may be an indication of the origin of both these components as organic or semi-organic carbonate.

To study the possible impact of oxygen-containing groups on the distribution of the discharge product, we have compared Li *1s* photoemission maps (normalized to the C *1s* signal) for the pristine and oxidized graphene at sequential discharge steps (Figure 2e,f). Finally, we found no essential differences in the product distribution, if pristine or oxidized graphene is used as the electrode. In both cases, product growth is lateral with the corresponding formation of a grid-like structure. This structure inherited neither the pristine graphene features nor the domain distribution in graphene that has a larger average size (about several microns). This can be seen from the C *1s* and O *1s* maps of the pristine electrode.

Summing up, we discovered that oxygen-containing groups on graphene (epoxy, carbonyl, and lactone) have no impact on the rate of one-electron ORR in aprotic media in the absence of metal cations. This is evidently due to the fact that their introduction practically does not vary DOS at the FL. At the same time, in Li^+-containing electrolytes, oxygen-containing groups on the graphene surface accelerate both second electron transfer and carbon degradation.

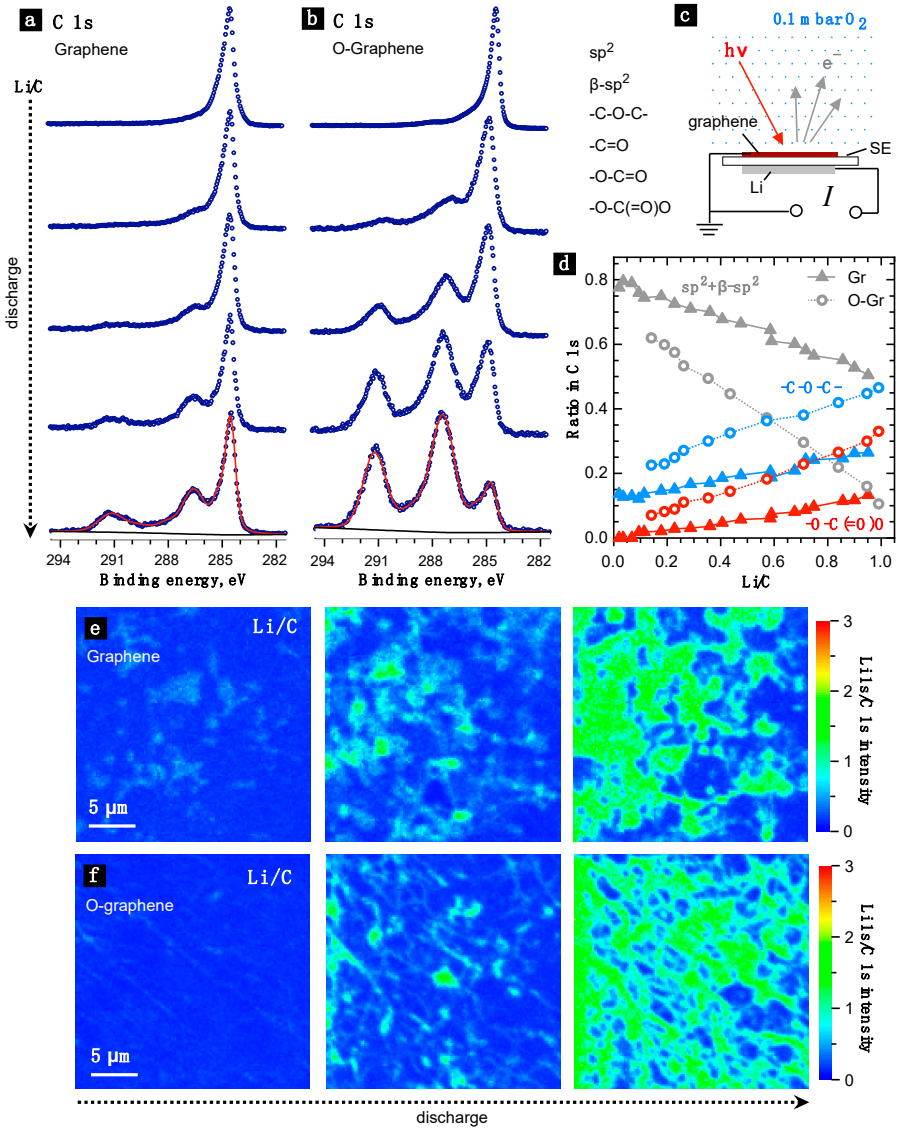

Figure 2. C *1s* core-level spectra at various stages of Li-O_2 cell discharge on (**a**) pristine and (**b**) oxidized graphene; (**c**) Li-O_2 cell scheme; (**d**) evolution of C *1s* components' ratios upon discharge for pristine and oxidized graphene; the evolution of photoemission maps of Li *1s* intensity normalized to C *1s* intensity from (**e**) graphene and (**f**) O-graphene electrode upon cell discharge [23]. Reprinted from Carbon, Volume 176, Pages 632–641, Copyright 2021, with permission from Elsevier.

3.2. Size and Support Effects Examined by Correlative Microscopy on Catalytically Active Metal Particles

If one had to name classical phenomena in heterogeneous catalysis, particle size and support effects would be among the most frequent answers [40–42]. Originally, they have been studied by ex situ methods (mostly by area-averaging spectroscopy and microscopy), both for applied as well as model catalysts, but the focus was recently shifted toward corresponding in situ studies [43,44]. Particularly, metal/oxide interfaces and undercoordinated atoms at step edges exhibited the highest activity [45–48]. In the example described below, the effect of different interfaces between Rh particles and support materials and the size of the Rh particles on catalytic water production was examined by in situ correlative microscopy. By imaging the same areas of the same catalyst with two different microscopies under the same reaction conditions, complementary pieces of information were provided in real time. Through spatially resolved evaluation of catalytic performance,

surface structure, and surface composition, particle size effects and interface phenomena were directly revealed.

On a planar Rh foil, catalytic water production had already been studied by combining low energy electron microscopy (LEEM), UV, and X-ray photoemission electron microscopy ((UV and X)PEEM) or SPEM [49,50]. In addition to characterizing the high and low activity steady states and bistability [51–53], this elucidated spatio-temporal phenomena, such as mono- and multifrequential self-sustaining oscillations [54] or coexisting multi-states [55]. The resulting thorough understanding of the reaction mechanism then allows using catalytic water formation as a test reaction to differentiate the high and low catalytic activity states, as well as size and interface effects.

Correlative microscopy of catalytic water production can also be applied to differently supported aggregates of Rh powder ("Rh black", size of ~5–30 μm) [56]. As a special twist, such Rh aggregates were applied to Rh, Au, or ZrO_2 supports and combined in a single sample (1×1 cm^2), which was studied in situ by combining local chemical information from SPEM and local reaction kinetics from PEEM. Unsupported Rh was mimicked by the Rh/Rh system, where the aggregates exhibited the same surface morphology (i.e., curved and stepped structure) as in the other supported systems. In an attempt to mimic an inert support, Rh/Au was prepared, but turned out as a model system for an inactive metal layer decorating active particles through surface alloying or site blocking [57]. Catalysts for water gas shift are often Cu-based with an Au modification [58], while steam reforming catalysts are often Ni-based with an Au or Cu modification [59], demonstrating the applications of such systems. Finally, as a typical metal/oxide combination, Rh/ZrO_2 was selected as it is active in H_2 oxidation [53,60], CO and CO_2 hydrogenation [61], or steam reforming [62]. Such systems, i.e., various oxides (including ZrO_2) supporting platinum group metals or other late transition metals, are also well-known for metal surfaces partially or fully decorated by oxide, i.e., strong metal/support interaction (SMSI) [63–68].

The experimental setup is illustrated in Figure 3. Catalytic water production was in situ visualized by PEEM as it occurred simultaneously on the three parts comprising the sample (Rh/Rh, Rh/Au, Rh/ZrO_2). The same regions of the same catalyst were studied under identical reaction conditions in situ by SPEM to yield chemical information with spatial resolution to be combined with the local kinetics.

Catalytic water production was first studied on Rh/Rh by PEEM visualization of the catalytically active and inactive states and kinetic transitions between them. For this reaction, before reacting, both reactants have to adsorb on the catalyst, i.e., it follows the Langmuir–Hinshelwood mechanism [51,69]. At low $p(H_2)/p(O_2)$, where the experiments always started, hydrogen adsorption was blocked by adsorbed oxygen and the sample was in the catalytically inactive state. This state is shown in Figure 4a for the quasi-unsupported Rh particles. While keeping $p(O_2)$ and T constant and increasing $p(H_2)$, at a certain $p(H_2)$ value, called τ_A, the sample turned catalytically active via a kinetic transition. On Rh/Rh, H_{ads} fronts spread over the entire field of view after nucleating at the particle perimeters [53] during such a kinetic transition as illustrated in Figure 4b. The system exhibited catalytic activity after the kinetic transition (Figure 4c), with a nearly adsorbate-free surface. A reverse kinetic transition, turning the sample catalytically inactive, took place upon decreasing $p(H_2)$. The corresponding $p(H_2)$ value, called τ_B, differed from τ_A, as characteristic of a bistable reaction [51–53]. PEEM is an ideal tool for visualizing these kinetic transitions as the PEEM image intensity is strongly governed by the surface coverage. The catalytically active surface, nearly free of adsorbates, exhibited a bright image contrast in PEEM due to its lower work function in comparison to adsorbate-covered Rh. In turn, the catalytically inactive surface appeared much darker due to the higher work function of the oxygen-covered surface. For comparison of Rh/Rh, Rh/Au, and Rh/ZrO_2, similarly sized Rh particles, having a diameter of ~20 μm, were selected and the local PEEM intensity was read out from the recorded video sequences.

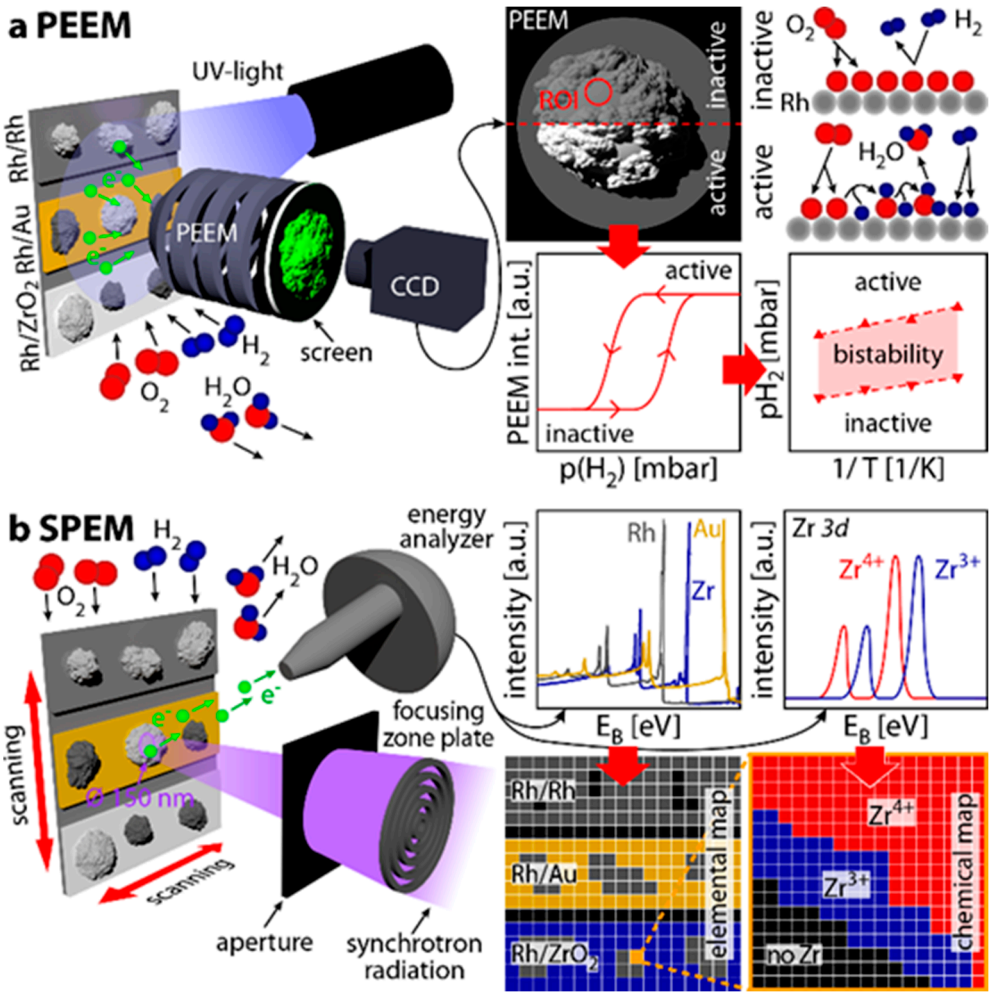

Figure 3. The correlative microscopy approach. (**a**) By illuminating the sample with UV light and directing the photoemitted electrons onto a fluorescent screen, an image is formed in PEEM. The catalytic activity, schematically displayed in the ball models, is indicated by the image brightness. Kinetic phase diagrams can be obtained by evaluating the hysteresis curves resulting from analysis of selected regions (ROIs) in the PEEM video sequences. (**b**) Elemental/chemical maps from nm to mm scale and local X-ray photoelectron spectra (XPS) in SPEM result from analysis of the energy of photoelectrons emitted while raster scanning the sample under a synchrotron X-ray beam. Reproduced from Ref. [56], published by American Chemical Society under a CC-BY-4.0 license. © 2023 The Authors.

Kinetic phase diagrams, constructed by evaluating a series of similar experiments repeated at different temperatures, are shown in Figure 4d. For Rh/Rh, for example, a "big" particle in the middle was analyzed as marked in Figure 4a. The shape of the kinetic phase diagrams of Rh/Rh (black) and Rh/Au (red) is similar, but Rh/Au exhibits both, τ_A and τ_B, at higher $p(H_2)$. This seems unusual since no interaction between the Au support and the Rh particles is expected and since (bulk) Au, due to no dissociative adsorption of the reactants taking place [70], is catalytically inactive in catalytic water production.

The τ_A and τ_B values for Rh/ZrO_2 (blue diagram) are also at higher $p(H_2)$ in comparison to Rh/Rh, but in addition, the sharp bend in the τ_A line observed for Rh/Rh and Rh/Au is not present. In previous work [53], the shift towards higher $p(H_2)$ was extensively discussed. In close vicinity of the metal/oxide interface, oxygen binding is energetically altered in comparison to the particle center. As the adsorption kinetics are governed by the adsorption energetics, this results in a shift towards oxygen in the local hydrogen/oxygen adsorption equilibrium, and thus higher $p(H_2)$ is necessary for inducing a kinetic transition.

The oxygen-induced surface restructuring, resulting in the sharply bent τ_A line for Rh/Rh and Rh/Au, appeared to be inhibited for Rh/ZrO_2 due to the metal/oxide interface.

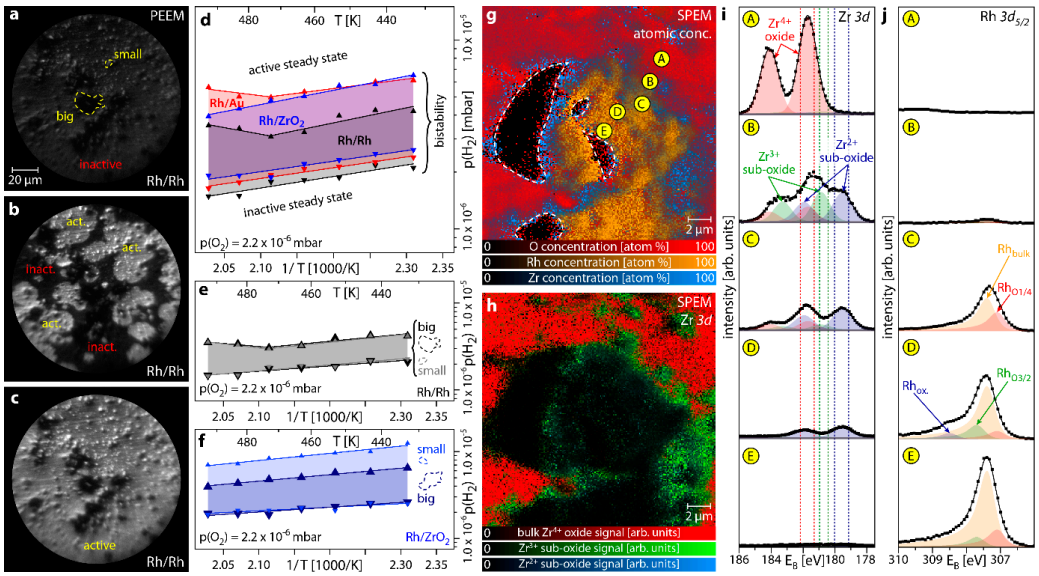

Figure 4. Particle size and support effects in catalytic water production on supported Rh particles. (**a**–**c**) In situ PEEM images of a kinetic transition from the catalytically inactive state to the catalytically active state for quasi-unsupported Rh particles at T = 443 K, $p(O_2) = 2.2 \times 10^{-6}$ mbar, $p(H_2) = 4.2 \times 10^{-6}$ mbar. Bright areas spreading from the boundaries of Rh particles correspond to an active water-producing surface, while dark areas indicate a catalytically inactive Rh surface; (**d**) kinetic phase diagram for temperatures from 433 K to 493 K for catalytic water production on "big" (~20 µm) Rh particles on Rh (black), Au (red) and ZrO_2 (blue) support while keeping $p(O_2)$ constant at 2.2×10^{-6} mbar; (**e**) kinetic phase diagram similar to (**d**) but for "big" (black diagram) and "small" (~5 µm) quasi-unsupported Rh particles (grey diagram); (**f**) kinetic phase diagram as in (**e**) but for "big" and "small" Rh particles supported by ZrO_2; (**g**) chemical map obtained by SPEM at T = 453 K, $p(O_2) = 2.2 \times 10^{-6}$ mbar, $p(H_2) = 4.0 \times 10^{-6}$ mbar for catalytically active Rh particles supported by ZrO_2, displaying the atomic composition of O (red), Rh (orange) and Zr (blue). Areas that were not imaged because of the setups' geometry are indicated by white dashed lines; (**h**) chemical map obtained by SPEM displaying Zr *3d* data for the same area as in (**g**). In addition to bulk zirconia (red), a Zr^{3+} sub-oxide (green) and a Zr^{2+} sub-oxide (blue) were present; (**i**) Zr *3d* XPS spectra were obtained at locations A to E marked in (**g**). The dashed lines indicate the energy windows employed in producing map (**h**); (**j**) Rh $3d_{5/2}$ XPS obtained at locations A to E marked in (**g**). Two components arising from different oxygen-bound Rh species (green and red) were present as well as Rh surface oxide (blue) and bulk Rh (orange). Adapted from Ref. [56], published by American Chemical Society under a CC-BY-4.0 license. © 2023 The Authors.

In the PEEM field of view, several particles of different sizes were present in addition to the "big" ones (Figure 4a–c). Due to the kinetic information conveyed in the in situ PEEM recordings, and the experimental conditions being inherently identical for all particle sizes due to the use of a microscopy technique, size effects could be directly addressed. A comparison of kinetic phase diagrams for "big" and additional "small" (~5 µm) Rh particles on Rh support is shown in Figure 4e. As expected, due to the lack of interface effects for this system, the diagrams were identical within the expected experimental accuracy. For Rh/Au, the same absence of size effects was observed. For Rh/ZrO_2, there was, however, a clear effect of the particle size: For the "small" particle, the τ_B values remained practically identical, while τ_A values at significantly higher $p(H_2)$ were observed. The metal/support interface was thus proven to determine the catalytic activity: For bigger particles, the ratio between particle surface area and perimeter/interface length is lower

in comparison to smaller particles, and thus stronger interface effects were observed for smaller particles.

While particle size and interface effects could unambiguously be shown by PEEM, detailed chemical information could not be provided. The SPEM hosted at the ESCA Microscopy beamline of the Elettra synchrotron was therefore used to gather these missing pieces of information and was operated with a photon energy of 720 eV. The unusual behavior of Rh/Au in the PEEM experiments could be explained based on SPEM: Au atoms were observed to migrate onto the Rh particle. As they were highly likely to be located at step edges of the Rh surfaces, as previously observed on various platinum group metals [57,71], crucial sites for dissociative adsorption of hydrogen on Rh were blocked [72]. Switching to the catalytically active state thus required higher $p(H_2)$ to compensate for the lower activity of step edges resulting from the RhAu alloy formation, leading to the observed shifted kinetic phase diagram.

Analogous results of the "big" ZrO_2-supported Rh particle obtained in situ in the catalytically active state are displayed in Figure 4g–j. A chemical map, derived from the O *1s*, Rh $3d_{5/2}$, and Zr *3d* signals, corrected for the differing X-ray cross-sections and inelastic mean free path lengths, displays the atomic composition of O (red), Rh (orange), and Zr (blue) (Figure 4g). Significant amounts of ZrO_x can be identified in the map to have been present on the Rh particle. The concentration of ZrO_x, however, decreased from the metal/oxide interface towards the center of the particle, where no ZrO_x was present. Furthermore, clearly different Zr/O atomic ratios (as much as 50%) were observed for the interfacial region (appearing blue) and the support (appearing purple). Based on previous XPS work on oxidized Zr [73,74] and on ZrO_x islands and thin films on Rh(111) [63], a Zr *3d* chemical map was constructed using three different Zr^{x+} species (Figure 4h). The contributions of the individual species to the absolute background-normalized Zr *3d* signal are shown in red (Zr^{4+} bulk-oxide), green (Zr^{3+} sub-oxide), and blue (Zr^{2+} sub-oxide) and reflect the trends observed in Figure 4g.

In Figure 4i,j corresponding high-resolution Zr *3d* and Rh $3d_{5/2}$ XPS spectra are displayed for five locations A to E which were placed starting on the zirconia and continuing along a line to the Rh particle center. In the Zr *3d* spectra (Figure 4i), the same three components as in the chemical map are displayed. In the Rh $3d_{5/2}$ spectra (Figure 4j), two components arising from different oxygen-bound Rh species ($Rh_{O2/3}$, green and $Rh_{O1/4}$, red), a component related to Rh surface oxide (Rh_{Ox}, blue) and bulk Rh (Rh_{bulk}, orange) were present, assigned based on previous work [49,55].

The complete picture was constructed by combining all pieces of information: bulk-like ZrO_2 was present at location A, i.e., several μm away from the particle on the zirconia support. Zr sub-oxides were present in addition at location B, i.e., near the metal/oxide interface but still on the support, but barely any Rh was present. As, e.g., reported for Pt or Rh particles on zirconia support [63,75], this hinted at hydrogen spillover taking place from the particle to the support, partially reducing ZrO_2. Still near the metal/support interface, but on the Rh particle, in turn, zirconium was present in significant amounts, mostly in the form of Zr sub-oxides, and catalytic activity of the surface was indicated by the $Rh_{O1/4}$ component (location C). The present Zr sub-oxides decreased upon moving towards the center of the particle (location D), but an unexpected distinct shoulder due to the presence of Rh surface was observed in the Rh $3d_{5/2}$ spectrum. Probably resulting from the enhanced oxygen binding in the vicinity of the metal/oxide interface [53,76], minute quantities of Zr sub-oxides were enhancing the oxidation of Rh. No Zr was present in the center of the particle and the Rh surface was catalytically active (location E).

An unexpected complexity of seemingly simple interfaces between metal and support was detected by SPEM. Significant amounts of Au from the support decorated the Rh particles because of the exceptional mobility of Au atoms and modified the catalytic properties by the formation of a RhAu surface alloy. A complex interfacial region stretching over several μm was formed in the Rh/ZrO_2 system, resulting from the occurrence of ZrO_x islands on the Rh particles, which resembled the states observed in strong metal/support interac-

tion (SMSI) on variously oxide-supported platinum group metal nanoparticles [63,64,66,68]. Furthermore, hydrogen spilling over from the Rh particles onto the ZrO_x support in the vicinity of the interface, resulting in the formation of substoichiometric Zr oxides, and a narrow region where Rh surface oxidation was enhanced paralleled the modification of oxygen binding near the metal/oxide interface, which was already previously reported [53,76], in combination leading to the reported modifications of the catalytic properties through support-induced effects (Figure 4).

In summary, catalytic water production, a model reaction also employed in several areas of technology, was imaged in situ by PEEM, focusing on the catalytic properties of Rh stepped particles on three support materials (Rh, Au, ZrO_2). As a result of differing particle sizes and varying support materials, the supported particles exhibited significantly modified catalytic properties, as determined by monitoring kinetic transitions between catalytically active and inactive states.

Using SPEM in a correlative way, i.e., by applying the same reaction conditions to the same catalysts, the results obtained by PEEM could be explained. Support material migrating onto the Rh particles was identified by SPEM as the cause of the differing catalytic behavior. An RhAu surface alloy was detected on Rh/Au and hydrogen spillover from the particles to the zirconia, causing substoichiometric Zr oxide formation, and enhanced oxidation of Rh was visualized for Rh/ZrO_2. The power of the correlative microscopy approach was convincingly demonstrated as the catalytic behavior of differently supported Rh particles could only be elucidated by combining the chemical information from SPEM with the real-time PEEM reactivity data.

A single sample comprising varying Rh particle sizes and several support materials acted as particle size and support library, which was investigated by combining two microscopy techniques, one providing local chemical information and the other one local reaction kinetics. Demonstrated using catalytic water formation on Rh, which is a well-understood reaction from a mechanistic perspective, the highlighted strategy could be extended to other technologically relevant reactions and used for benchmarking particle size and interface effects in catalysis.

3.3. Correlative Microscopy for Nanoscale Exploration of Structure-Function Relationships in Catalytic Materials

The composition and structure of the first few surface layers of a catalyst govern how it engages and evolves in a chemical reaction. Typically, real materials evolve heterogeneously during a reaction as a consequence of their micro- and defect structure. Effects such as preferential oxidation of crystallographic facets, diffusion of reactants along crystallographic defects, or solute segregation can result in spatially varying chemical properties due to a non-homogeneous electronic structure across the surface [77,78]. This inhomogeneity directly impacts the interfacial interaction energetics, conversion rates, and, in the case of electrocatalysts, the potential distribution that eventually controls the reactivity and stability. It is crucial to have characterization tools available that resolve features at the appropriate length scale and sensitivity to establish relationships between structure and catalytic behavior. This work demonstrates how to combine SPEM and atom probe tomography (APT) at an identical location to interrogate the structure, chemical state, and composition of surface and sub-surface regions of catalytic materials. While APT provides unprecedented insights into the nanoscale surface chemistry in three dimensions, the complementary information about the surface oxidation states is assessed by SPEM. This study focuses on Ir-Ru alloys and their thermal oxides, which are promising materials for the anodic oxygen evolution reaction (OER) in proton exchange membrane electrolyzers, as they combine the longevity of IrO_2 and high electrocatalytic activity of RuO_2 towards the OER [79–84].

To enable the correlative microscopy approach, approximately 100 nm thick Ir-Ru alloy thin films were directly deposited onto pre-cleaned commercial flat-top coupons [85] (Cameca/Ametek, Inc.; Figure 5a), commonly used as support for APT specimen prepara-

tion. The oxide samples were prepared by annealing the alloy in air at 600 °C for 5 h to produce an oxide thickness > 10 nm.

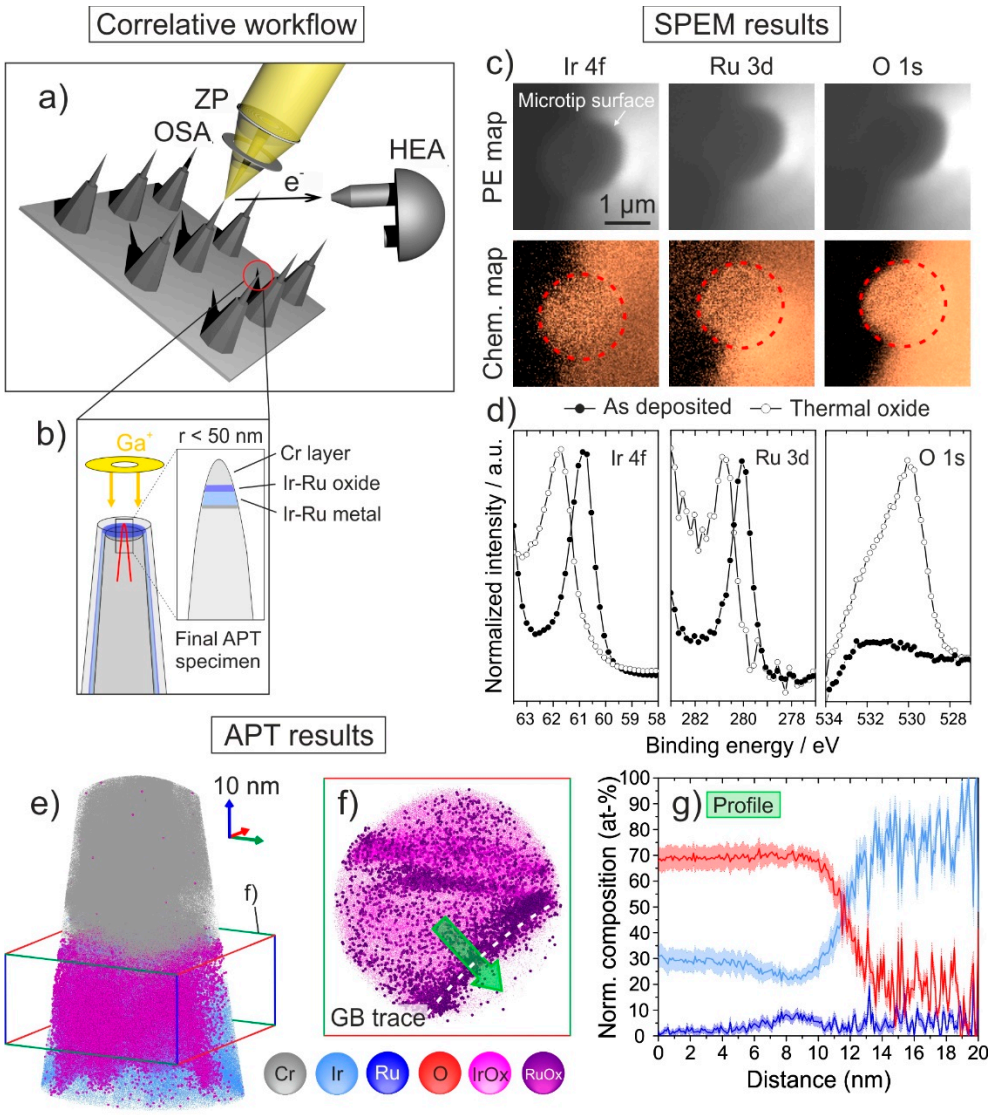

Figure 5. (**a**) SPEM measurement principle on the top surface of an individual microtip. (**b**) FIB-SEM annular milling of microtip. Final APT specimen features top surface measured with SPEM. (**c**) Photoelectron (PE) and corresponding chemical maps of relevant core level lines obtained by SPEM. (**d**) Comparison of core level spectra obtained from as-deposited (filled symbols), and thermally oxidized (hollow symbol) samples extracted from PE maps. Spectra are restricted to one peak of doublet due to detector resolution. (**e**) Three-dimensional APT reconstruction of thermally oxidized sample. The box indicates the region illustrated in top-down view in (**f**), which reveals heterogeneous Ru distribution within the oxide with strong segregation of Ru to grain boundaries. The compositional profile across the GB in (**g**) shows a less oxidized grain showcasing selective oxidation of the material (reproduced and modified from [86], open-access license).

The approximately 2 µm wide flat-top surfaces of the microtips on the coupons hosting the alloy/oxide were examined with SPEM (imaging mode) using a photon energy of about $h\nu$ = 650 eV. After SPEM inspection, the surfaces were protected with a Cr layer of 300 nm (electron beam PVD), before needle-shaped APT specimens were prepared by annular milling using a dual beam focused-ion beam SEM (Figure 5b). Special care was taken that the surface analyzed with SPEM is part of the analyzed APT volume. APT specimens were analyzed with a CAMECA LEAP 5000XR instrument.

Further experimental details can be found in the original publication [86].

In contrast to similar experimental techniques (e.g., XPEEM), SPEM imposes little constraints regarding applicable surface geometries enabling the direct imaging and measurement of the flat-top surface of individual microtips (Figure 5c). The chemical maps of the Ir *4f*, Ru *3d*, and O *1s* core levels obtained from the thermal oxide (Figure 5d) reveal no lateral chemical heterogeneities across the flat-top surface on the probed length scale. The averaged spectra extracted from the flat-top area of the images reveal a distinct oxidation of both metal core levels from 60.9 eV to 61.8 eV for Ir $4f_{7/2}$, and from 280.0 eV to 280.8 eV for Ru $3d_{5/2}$, both consistent with metallic and +IV oxidation states, respectively. The main O *1s* peak at 529.8 eV obtained from the oxide coincides with the lattice oxygen binding energy of Ir-Ru mixed oxides with a Ru content < 25 at%, consistent with the present average alloy composition of $Ir_{0.92}Ru_{0.08}$, as determined by APT. It should be noted that the measurement of beam-sensitive materials such as these thin oxide layers benefits from the short dwell time realizable in the snapshot mode of the SPEM.

The APT analysis of the surface shown in Figure 5c,d reveals a richer picture of the underlying microstructure of the oxide (Figure 5e,f). The analysis starts in the Cr protection layer and continues through the oxide layer down to the metallic Ir-Ru thin film. APT enables the quantification of Ru segregation to grain boundaries (GB), likely a result of free energy minimization during the synthesis of the alloy. The analysis shows that the intragrain composition is $Ir_{0.94}Ru_{0.05}O_2$, while RuO_2-enriched GBs fluctuate between $Ir_{0.75}Ru_{0.25}O_2$ and $Ir_{0.40}Ru_{0.60}O_2$. Interestingly, certain grains developed fully stoichiometric oxides, while others remained essentially in a metallic state as revealed by the composition profile across a GB in Figure 5f,g. The high spatial resolution of APT can well resolve local chemical differences at the nanoscale, which might exhibit a different catalytic activity than the average composition of the material.

This proof-of-concept work demonstrated the feasibility of combining SPEM and APT at an identical location to obtain a more complete picture of the surface of a catalytic material. Both methods have yielded consistent results in terms of determined oxide stoichiometry and oxidation states despite the difference in probing length scale. The established methodological approach forms the basis for further mechanistic studies with model systems with feature sizes resolvable with SPEM to truly link small, individual entities on complex surfaces to their functional impact on solute distribution, ordering, electronic structure, and reactivity. SPEM's capability to accommodate in situ experiments under near-ambient pressure or electrochemical conditions will support the mission to establish a scientific ground for the informed bottom-up engineering of more sustainable functional interfaces.

4. Conclusions

SPEM is one of the approaches that allowed combining X-ray photoelectron spectroscopy with sub-micron spatial resolution; the instrument hosted at the Elettra synchrotron facility over the years has been upgraded to fulfill the increasingly demanding needs of in situ and operando experiments. This technique is particularly helpful for the investigation of modern catalytic materials where understanding surface–interfacial properties requires essential factors such as the atomic arrangements, compositional and chemical profiles, and, more importantly, their response to external stimuli such as temperature, electric and magnetic fields, light and gas exposure, etc., at the nanoscale. In this manuscript, we reported a few examples showing the capabilities of the SPEM at Elettra in the investigation of catalytic materials in different conditions and processes: oxygen reduction reactions (ORR) on electrochemical cells to study the electrochemical properties of graphene, size and support effects of catalytically active Rh metal particles on different substrates to study the inactive and active states in the H_2 oxidation reaction, and an example of correlative microscopy for nanoscale exploration of structure–function relationships in catalytic materials were the main scientific topics addressed in the work.

Author Contributions: Conceptualization, L.G., M.A. and Z.M.; investigation, L.G., M.A., L.V.Y., P.W., G.R. and K.S.; data curation, L.V.Y., P.W., G.R. and K.S.; writing—review and editing, L.G., M.A., L.V.Y., P.W., G.R. and K.S. All authors have read and agreed to the published version of the manuscript.

Funding: This research was funded in part by the Austrian Science Fund (FWF) [10.55776/F81].

Data Availability Statement: At the time of publication of this manuscript, no research data are publicly available.

Acknowledgments: We acknowledge Elettra Sincrotrone Trieste for providing access to its synchrotron radiation facilities. Contributions by M. Raab: J. Zeininger, Y. Suchorski, M. Stöger-Pollach, L.M. Rois, and R. Parmar are gratefully acknowledged.

Conflicts of Interest: The authors declare no conflict of interest. Author Kevin Sparwasser was employed by the company Max-Planck-Institut für Eisenforschung GmbH. The research was conducted in the absence of any commercial or financial relationships that could be construed as a potential conflict of interest.

References

1. Schlögl, R. Heterogeneous Catalysis. *Angew. Chemie Int. Ed.* **2015**, *54*, 3465–3520. [CrossRef] [PubMed]
2. Rupprechter, G. Operando Surface Spectroscopy and Microscopy during Catalytic Reactions: From Clusters via Nanoparticles to Meso-Scale Aggregates. *Small* **2021**, *17*, 2004289. [CrossRef] [PubMed]
3. Zhong, L.; Chen, D.; Zafeiratos, S. A mini review of in situ near-ambient pressure XPS studies on non-noble, late transition metal catalysts. *Catal. Sci. Technol.* **2019**, *9*, 3851–3867. [CrossRef]
4. Roy, K.; Artiglia, L.; Van Bokhoven, J.A. Ambient Pressure Photoelectron Spectroscopy: Opportunities in Catalysis from Solids to Liquids and Introducing Time Resolution. *ChemCatChem* **2018**, *10*, 666–682. [CrossRef]
5. Meirer, F.; Weckhuysen, B.M. Spatial and temporal exploration of heterogeneous catalysts with synchrotron radiation. *Nat. Rev. Mater.* **2018**, *3*, 324–340. [CrossRef]
6. Sheng, B.; Cao, D.; Liu, C.; Chen, S.; Song, L. Support Effects in Electrocatalysis and Their Synchrotron Radiation-Based Characterizations. *J. Phys. Chem. Lett.* **2021**, *12*, 11543–11554. [CrossRef]
7. Somorjai, G.A.; Rupprechter, G. The Flexible Surface: Molecular Studies Explain the Extraordinary Diversity of Surface Chemical Properties. *J. Chem. Educ.* **1998**, *75*, 161. [CrossRef]
8. Ade, H.; Kirz, J.; Hulbert, S.; Johnson, E.; Anderson, E.; Kern, D. Scanning photoelectron microscope with a zone plate generated microprobe. *Nucl. Instrum. Methods Phys. Res. Sect. A* **1990**, *291*, 126–131. [CrossRef]
9. Ade, H.; Smith, A.; Zhang, H.; Zhuang, G.; Kirz, J.; Rightor, E.; Hitchcock, A. X-ray spectromicroscopy of polymers and tribological surfaces at beamline X1A at the NSLS. *J. Electron Spectros. Relat. Phenomena* **1997**, *84*, 53–72. [CrossRef]
10. Hayes Griffith, O.; Engel, W. Historical perspective and current trends in emission microscopy, mirror electron microscopy and low-energy electron microscopy. *Ultramicroscopy* **1991**, *36*, 1–28. [CrossRef]
11. Horiba, K.; Nakamura, Y.; Nagamura, N.; Toyoda, S.; Kumigashira, H.; Oshima, M.; Amemiya, K.; Senba, Y.; Ohashi, H. Scanning photoelectron microscope for nanoscale three-dimensional spatial-resolved electron spectroscopy for chemical analysis. *Rev. Sci. Instrum.* **2011**, *82*, 113701. [CrossRef] [PubMed]
12. Dudin, P.; Lacovig, P.; Fava, C.; Nicolini, E.; Bianco, A.; Cautero, G.; Barinov, A. Angle-resolved photoemission spectroscopy and imaging with a submicrometre probe at the SPECTROMICROSCOPY-3.2L beamline of Elettra. *J. Synchrotron Radiat.* **2010**, *17*, 445–450. [CrossRef] [PubMed]
13. Sezen, H.; Alemán, B.; Amati, M.; Dalmiglio, M.; Gregoratti, L. Spatially resolved chemical characterization with scanning photoemission spectromicroscopy: Towards near-ambient-pressure experiments. *ChemCatChem* **2015**, *7*, 3665–3673. [CrossRef]
14. Kaulich, B.; Thibault, P.; Gianoncelli, A.; Kiskinova, M. Transmission and emission X-ray microscopy: Operation modes, contrast mechanisms and applications. *J. Phys. Condens. Matter.* **2011**, *23*, 083002. [CrossRef] [PubMed]
15. Amati, M.; Barinov, A.; Gregoratti, L.; Sezen, H.; Kiskinova, M. Scanning Photoelectron Microscopy: Past, Present and Future. In *Springer Handbook of Surface Science*; Springer: Berlin/Heidelberg, Germany, 2020; pp. 427–448. [CrossRef]
16. Abyaneh, M.K.M.K.; Gregoratti, L.; Amati, M.; Dalmiglio, M.; Kiskinova, M. Scanning Photoelectron Microscopy: A Powerful Technique for Probing Micro and Nano-Structures. *E-J. Surf. Sci. Nanotechnol.* **2011**, *9*, 158–162. [CrossRef]
17. Amati, M.; Susi, T.; Jovičević-Klug, P.; Jovičević-Klug, M.; Kosmala, T.; Granozzi, G.; Agnoli, S.; Yang, P.; Zhang, Y.; Scardamaglia, M.; et al. Scanning photoelectron spectromicroscopy: From static to operando studies of functional materials. *J. Electron Spectros. Relat. Phenomena.* **2023**, *265*, 147336. [CrossRef]
18. Attwood, D. *Soft X-rays and Extreme Ultraviolet Radiation: Principles and Applications*; Cambridge University Press: Cambridge, UK, 1999. [CrossRef]
19. Gregoratti, L.; Barinov, A.; Benfatto, E.; Cautsro, G.; Fava, C.; Lacovig, P.; Lonza, D.; Kiskinova, M.; Tommasini, R.; Mähl, S.; et al. 48-Channel electron detector for photoemission spectroscopy and microscopy. *Rev. Sci. Instrum.* **2004**, *75*, 64–68. [CrossRef]
20. Carrette, L.; Friedrich, K.A.; Stimming, U. Fuel Cells-Fundamentals and Applications. *Fuel Cells* **2001**, *1*, 5–39. [CrossRef]

21. Cheng, F.; Chen, J. Metal–air batteries: From oxygen reduction electrochemistry to cathode catalysts. *Chem. Soc. Rev.* **2012**, *41*, 2172. [CrossRef]
22. Padbury, R.; Zhang, X. Lithium–oxygen batteries—Limiting factors that affect performance. *J. Power Sources* **2011**, *196*, 4436–4444. [CrossRef]
23. Inozemtseva, A.I.; Kataev, E.Y.; Frolov, A.S.; Amati, M.; Gregoratti, L.; Beranová, K.; Dieste, V.P.; Escudero, C.; Fedorov, A.; Tarasov, A.V.; et al. On the catalytic and degradative role of oxygen-containing groups on carbon electrode in non-aqueous ORR. *Carbon N. Y.* **2021**, *175*, 632–641. [CrossRef]
24. Chang, Z.; Xu, J.; Zhang, X. Recent Progress in Electrocatalyst for Li-O_2 Batteries. *Adv. Energy Mater.* **2017**, *7*, 1700875. [CrossRef]
25. Šljukić, B.; Banks, C.E.; Compton, R.G. An overview of the electrochemical reduction of oxygen at carbon-based modified electrodes. *J. Iran. Chem. Soc.* **2005**, *2*, 1–25. [CrossRef]
26. Cline, K.K.; McDermott, M.T.; McCreery, R.L. Anomalously Slow Electron Transfer at Ordered Graphite Electrodes: Influence of Electronic Factors and Reactive Sites. *J. Phys. Chem.* **1994**, *98*, 5314–5319. [CrossRef]
27. Navalon, S.; Dhakshinamoorthy, A.; Alvaro, M.; Antonietti, M.; García, H. Active sites on graphene-based materials as metal-free catalysts. *Chem. Soc. Rev.* **2017**, *46*, 4501–4529. [CrossRef]
28. Zhang, J.; Xia, Z.; Dai, L. Carbon-based electrocatalysts for advanced energy conversion and storage. *Sci. Adv.* **2015**, *1*, e1500564. [CrossRef]
29. Chai, G.-L.; Hou, Z.; Ikeda, T.; Terakura, K. Two-Electron Oxygen Reduction on Carbon Materials Catalysts: Mechanisms and Active Sites. *J. Phys. Chem. C* **2017**, *121*, 14524–14533. [CrossRef]
30. Xu, Y.; Shelton, W.A. Oxygen Reduction by Lithium on Model Carbon and Oxidized Carbon Structures. *J. Electrochem. Soc.* **2011**, *158*, A1177. [CrossRef]
31. Dobrota, A.S.; Pašti, I.A.; Mentus, S.V.; Skorodumova, N.V. A DFT study of the interplay between dopants and oxygen functional groups over the graphene basal plane–implications in energy-related applications. *Phys. Chem. Chem. Phys.* **2017**, *19*, 8530–8540. [CrossRef]
32. Allouche, A.; Ferro, Y. Dissociative adsorption of atmospheric molecules at vacancies on the graphite (0001) surface of samples exposed to plasma. *J. Nucl. Mater.* **2007**, *363–365*, 117–121. [CrossRef]
33. Lee, S.M.; Lee, Y.H.; Hwang, Y.G.; Hahn, J.R.; Kang, H. Defect-Induced Oxidation of Graphite. *Phys. Rev. Lett.* **1999**, *82*, 217–220. [CrossRef]
34. Orudzhev, F.; Sobola, D.; Ramazanov, S.; Částková, K.; Papež, N.; Selimov, D.A.; Abdurakhmanov, M.; Shuaibov, A.; Rabadanova, A.; Gulakhmedov, R.; et al. Piezo-Enhanced Photocatalytic Activity of the Electrospun Fibrous Magnetic PVDF/$BiFeO_3$ Membrane. *Polymers* **2023**, *15*, 246. [CrossRef]
35. Orudzhev, F.; Ramazanov, S.; Sobola, D.; Kaspar, P.; Trčka, T.; Částková, K.; Kastyl, J.; Zvereva, I.; Wang, C.; Selimov, D.; et al. Ultrasound and water flow driven piezophototronic effect in self-polarized flexible α-Fe_2O_3 containing PVDF nanofibers film for enhanced catalytic oxidation. *Nano Energy* **2021**, *90*, 106586. [CrossRef]
36. Itkis, D.M.; Semenenko, D.A.; Kataev, E.Y.; Belova, A.I.; Neudachina, V.S.; Sirotina, A.P.; Havecker, M.; Teschner, D.; Knop-Gericke, A.; Dudin, P.; et al. Reactivity of Carbon in Lithium–Oxygen Battery Positive Electrodes. *Nano Lett.* **2013**, *13*, 4697–4701. [CrossRef]
37. Kapitanova, O.O.; Kataev, E.Y.; Usachov, D.Y.; Sirotina, A.P.; Belova, A.I.; Sezen, H.; Amati, M.; Al-Hada, M.; Gregoratti, L.; Barinov, A.; et al. Laterally Selective Oxidation of Large-Scale Graphene with Atomic Oxygen. *J. Phys. Chem. C* **2017**, *121*, 27915–27922. [CrossRef]
38. Inozemtseva, A.; Rulev, A.; Zakharchenko, T.; Isaev, V.; Yashina, L.; Itkis, D. Chemistry of Li-air batteries. *J. Electrochem. Soc.* **2023**, *159*, 324–362. [CrossRef]
39. Zakharchenko, T.K.; Belova, A.I.; Frolov, A.S.; Kapitanova, O.O.; Velasco-Velez, J.-J.; Knop-Gericke, A.; Vyalikh, D.; Itkis, D.M.; Yashina, L.V. Notable Reactivity of Acetonitrile Towards Li_2O_2/LiO_2 Probed by NAP XPS During Li–O_2 Battery Discharge. *Top. Catal.* **2018**, *61*, 2114–2122. [CrossRef]
40. Boudart, M. Catalysis by Supported Metals. *Adv. Catal.* **1969**, *20*, 153–166. [CrossRef]
41. Hayek, K.; Kramer, R.; Paál, Z. Metal-support boundary sites in catalysis. *Appl. Catal. A Gen.* **1997**, *162*, 1–15. [CrossRef]
42. Tuxen, A.; Carenco, S.; Chintapalli, M.; Chuang, C.H.; Escudero, C.; Pach, E.; Jiang, P.; Borondics, F.; Beberwyck, B.; Alivisatos, A.P.; et al. Size-Dependent Dissociation of Carbon Monoxide on Cobalt Nanoparticles. *J. Am. Chem. Soc.* **2013**, *135*, 2273–2278. [CrossRef]
43. Besenbacher, F.; Lauritsen, J.V.; Wendt, S. STM studies of model catalysts. *Nano Today* **2007**, *2*, 30–39. [CrossRef]
44. Liu, J. Advanced Electron Microscopy of Metal–Support Interactions in Supported Metal Catalysts. *ChemCatChem* **2011**, *3*, 934–948. [CrossRef]
45. Silvestre-Albero, J.; Rupprechter, G.; Freund, H.J. Atmospheric pressure studies of selective 1,3-butadiene hydrogenation on well-defined Pd/Al2O3/NiAl(110) model catalysts: Effect of Pd particle size. *J. Catal.* **2006**, *240*, 58–65. [CrossRef]
46. Jørgensen, M.; Grönbeck, H. Scaling Relations and Kinetic Monte Carlo Simulations to Bridge the Materials Gap in Heterogeneous Catalysis. *ACS Catal.* **2017**, *7*, 5054–5061. [CrossRef]
47. Vogt, C.; Groeneveld, E.; Kamsma, G.; Nachtegaal, M.; Lu, L.; Kiely, C.J.; Berben, P.H.; Meirer, F.; Weckhuysen, B.M. Unravelling structure sensitivity in CO_2 hydrogenation over nickel. *Nat. Catal.* **2018**, *1*, 127–134. [CrossRef]
48. Zeininger, J.; Raab, M.; Suchorski, Y.; Buhr, S.; Stöger-Pollach, M.; Bernardi, J.; Rupprechter, G. Reaction Modes on a Single Catalytic Particle: Nanoscale Imaging and Micro-Kinetic Modeling. *ACS Catal.* **2022**, *12*, 12774–12785. [CrossRef]

49. Winkler, P.; Zeininger, J.; Suchorski, Y.; Stöger-Pollach, M.; Zeller, P.; Amati, M.; Gregoratti, L.; Rupprechter, G. How the anisotropy of surface oxide formation influences the transient activity of a surface reaction. *Nat. Commun.* **2021**, *12*, 1–8. [CrossRef]
50. Zeininger, J.; Winkler, P.; Raab, M.; Suchorski, Y.; Prieto, M.J.; Tanase, L.C.; de Souza Caldas, L.; Tiwari, A.; Schmidt, T.; Stoger-Pollach, M. Pattern Formation in Catalytic H_2 Oxidation on Rh: Zooming in by Correlative Microscopy. *ACS Catal.* **2022**, *12*, 11974–11983. [CrossRef]
51. Schaak, A.; Imbihl, R. Bistability and formation of low work function areas in the O_2+H_2 reaction on a Rh(111) surface. *J. Chem. Phys.* **2000**, *113*, 9822–9829. [CrossRef]
52. Visart de Bocarmé, T.; Bär, T.; Kruse, N. In situ dynamic study of hydrogen oxidation on rhodium. *Ultramicroscopy* **2001**, *89*, 75–82. [CrossRef] [PubMed]
53. Suchorski, Y.; Datler, M.; Bespalov, I.; Freytag, C.; Zeininger, J.; Rupprechter, G. Transmitting metal–oxide interaction by solitary chemical waves: H_2 oxidation on ZrO_2 supported Rh. *Surf. Sci.* **2019**, *679*, 163–168. [CrossRef]
54. Suchorski, Y.; Datler, M.; Bespalov, I.; Zeininger, J.; Stöger-Pollach, M.; Bernardi, J.; Grönbeck, H.; Rupprechter, G. Visualizing catalyst heterogeneity by a multifrequential oscillating reaction. *Nat. Commun.* **2018**, *9*, 600. [CrossRef]
55. Winkler, P.; Zeininger, J.; Raab, M.; Suchorski, Y.; Steiger-Thirsfeld, A.; Stöger-Pollach, M.; Amati, M.; Gregoratti, L.; Grönbeck, H.; Rupprechter, G. Coexisting multi-states in catalytic hydrogen oxidation on rhodium. *Nat. Commun.* **2021**, *12*, 6517. [CrossRef]
56. Winkler, P.; Raab, M.; Zeininger, J.; Rois, L.M.; Suchorski, Y.; Stöger-Pollach, M.; Amati, M.; Parmar, R.; Gregoratti, L.; Rupprechter, G. Imaging Interface and Particle Size Effects by In Situ Correlative Microscopy of a Catalytic Reaction. *ACS Catal.* **2023**, *13*, 7650–7660. [CrossRef] [PubMed]
57. Dahl, S.; Logadottir, A.; Egeberg, R.C.; Larsen, J.H.; Chorkendorff, I.; Törnqvist, E.; Nørskov, J.K. Role of Steps in N2 Activation on Ru(0001). *Phys. Rev. Lett.* **1999**, *83*, 1814–1817. [CrossRef]
58. Santos, J.L.; Reina, T.R.; Ivanova, S.; Centeno, M.A.; Odriozola, J.A. Gold promoted $Cu/ZnO/Al_2O_3$ catalysts prepared from hydrotalcite precursors: Advanced materials for the WGS reaction. *Appl. Catal. B Environ.* **2017**, *201*, 310–317. [CrossRef]
59. Besenbacher, F.; Chorkendorff, I.; Clausen, B.S.; Hammer, B.; Molenbroek, A.M.; Nørskov, J.K.; Stensgaard, I. Design of a Surface Alloy Catalyst for Steam Reforming. *Science* **1998**, *279*, 1913–1915. [CrossRef]
60. Frey, H.; Beck, A.; Huang, X.; van Bokhoven, J.A.; Willinger, M.G. Dynamic interplay between metal nanoparticles and oxide support under redox conditions. *Science* **2022**, *376*, 982–987. [CrossRef]
61. Boffa, A.; Lin, C.; Bell, A.T.; Somorjai, G.A. Promotion of CO and CO_2 Hydrogenation over Rh by Metal Oxides: The Influence of Oxide Lewis Acidity and Reducibility. *J. Catal.* **1994**, *149*, 149–158. [CrossRef]
62. Igarashi, A.; Ohtaka, T.; Honnma, T.; Fukuhara, C. The Role of Zirconium Dioxide in the Activation of Water and as the Catalytic Site for Low-Temperature Steam Reforming Over Rh/ZrO_2. In *Studies in Surface Science and Catalysis*; Elsevier: Amsterdam, The Netherlands, 1993; pp. 2083–2086. [CrossRef]
63. Lackner, P.; Choi, J.I.J.; Diebold, U.; Schmid, M. Substoichiometric ultrathin zirconia films cause strong metal–support interaction. *J. Mater. Chem. A* **2019**, *7*, 24837–24846. [CrossRef]
64. Bernal, S.; Calvino, J.; Cauqui, M.; Gatica, J.; Larese, C.; Omil, J.P.; Pintado, J. Some recent results on metal/support interaction effects in NM/CeO_2 (NM: Noble metal) catalysts. *Catal. Today* **1999**, *50*, 175–206. [CrossRef]
65. Fu, Q.; Wagner, T.; Olliges, S.; Carstanjen, H.-D. Metal−Oxide Interfacial Reactions: Encapsulation of Pd on TiO_2 (110). *J. Phys. Chem. B* **2005**, *109*, 944–951. [CrossRef]
66. Willinger, M.G.; Zhang, W.; Bondarchuk, O.; Shaikhutdinov, S.; Freund, H.; Schlögl, R. A Case of Strong Metal–Support Interactions: Combining Advanced Microscopy and Model Systems to Elucidate the Atomic Structure of Interfaces. *Angew. Chemie Int. Ed.* **2014**, *53*, 5998–6001. [CrossRef]
67. Liu, Z.; Grinter, D.C.; Lustemberg, P.G.; Nguyen-Phan, T.D.; Zhou, Y.; Luo, S.; Waluyo, I.; Crumlin, E.J.; Stacchiola, D.J.; Zhou, J.; et al. Dry Reforming of Methane on a Highly-Active $Ni-CeO_2$ Catalyst: Effects of Metal-Support Interactions on C−H Bond Breaking. *Angew. Chemie Int. Ed.* **2016**, *55*, 7455–7459. [CrossRef]
68. Li, Y.; Zhang, Y.; Qian, K.; Huang, W. Metal–Support Interactions in Metal/Oxide Catalysts and Oxide–Metal Interactions in Oxide/Metal Inverse Catalysts. *ACS Catal.* **2022**, *12*, 1268–1287. [CrossRef]
69. Yates, J.T.; Thiel, P.A.; Weinberg, W.H. The catalytic reaction between adsorbed oxygen and hydrogen on Rh(111). *Surf. Sci.* **1979**, *82*, 45–68. [CrossRef]
70. Sault, A.G.; Madix, R.J.; Campbell, C.T. Adsorption of oxygen and hydrogen on Au(110)-(1 × 2). *Surf. Sci.* **1986**, *169*, 347–356. [CrossRef]
71. Óvári, L.; Berkó, A.; Vári, G.; Gubó, R.; Farkas, A.P.; Kónya, Z. The growth and thermal properties of Au deposited on Rh(111): Formation of an ordered surface alloy. *Phys. Chem. Chem. Phys.* **2016**, *18*, 25230–25240. [CrossRef]
72. Africh, C.; Esch, F.; Li, W.X.; Corso, M.; Hammer, B.; Rosei, R.; Comelli, G. Two-Step Reaction on a Strained, Nanoscale Segmented Surface. *Phys. Rev. Lett.* **2004**, *93*, 126104. [CrossRef] [PubMed]
73. Bespalov, I.; Datler, M.; Buhr, S.; Rachael, W.; Rupprechter, G.; Suchorski, Y. Initial stages of oxide formation on the Zr surface at low oxygen pressure: An in situ FIM and XPS study. *Ultramicroscopy* **2015**, *159*, 147–151. [CrossRef] [PubMed]
74. Ma, W.; Herbert, F.W.; Senanayake, S.D.; Yildiz, B. Non-equilibrium oxidation states of zirconium during early stages of metal oxidation. *Appl. Phys. Lett.* **2015**, *106*, 101603. [CrossRef]
75. Hoang, D.-L.; Berndt, H.; Lieske, H. Hydrogen spillover phenomena on Pt/ZrO_2. *Catal. Lett.* **1995**, *31*, 165–172. [CrossRef]

76. Suchorski, Y.; Kozlov, S.M.; Bespalov, I.; Datler, M.; Vogel, D.; Budinska, Z.; Neyman, K.M.; Rupprechter, G. The role of metal/oxide interfaces for long-range metal particle activation during CO oxidation. *Nat. Mater.* **2018**, *17*, 519–522. [CrossRef] [PubMed]
77. Schweinar, K.; Beeg, S.; Hartwig, C.; Rajamathi, C.R.; Kasian, O.; Piccinin, S.; Prieto, M.J.; Tanase, L.C.; Gottlob, D.M.; Schmidt, T.; et al. Formation of a 2D Meta-stable Oxide by Differential Oxidation of AgCu Alloys. *ACS Appl. Mater. Interfaces.* **2020**, *12*, 23595–23605. [CrossRef] [PubMed]
78. Amati, M.; Gregoratti, L.; Zeller, P.; Greiner, M.; Scardamaglia, M.; Junker, B.; Ruß, T.; Weimar, U.; Barsan, N.; Favaro, M.; et al. Near ambient pressure photoelectron spectro-microscopy: From gas-solid interface to operando devices. *J. Phys. D. Appl. Phys.* **2021**, *54*, 204004. [CrossRef]
79. Kasian, O.; Geiger, S.; Stock, P.; Polymeros, G.; Breitbach, B.; Savan, A.; Ludwig, A.; Cherevko, S.; Mayrhofer, K.J.J. On the Origin of the Improved Ruthenium Stability in RuO_2–IrO_2 Mixed Oxides. *J. Electrochem. Soc.* **2016**, *163*, F3099–F3104. [CrossRef]
80. Lahn, L.; Mingers, A.M.; Savan, A.; Ludwig, A.; Kasian, O. Low Ti Additions to Stabilize Ru-Ir Electrocatalysts for the Oxygen Evolution Reaction. *ChemElectroChem* **2024**, *11*, e202300399. [CrossRef]
81. Saveleva, V.A.; Wang, L.; Luo, W.; Zafeiratos, S.; Ulhaq-Bouillet, C.; Gago, A.S.; Friedrich, K.A.; Savinova, E.R. Uncovering the Stabilization Mechanism in Bimetallic Ruthenium–Iridium Anodes for Proton Exchange Membrane Electrolyzers. *J. Phys. Chem. Lett.* **2016**, *7*, 3240–3245. [CrossRef]
82. Danilovic, N.; Subbaraman, R.; Chang, K.C.; Chang, S.H.; Kang, Y.; Snyder, J.; Paulikas, A.P.; Strmcnik, D.; Kim, Y.T.; Myers, D.; et al. Using Surface Segregation To Design Stable Ru-Ir Oxides for the Oxygen Evolution Reaction in Acidic Environments. *Angew. Chemie Int. Ed.* **2014**, *53*, 14016–14021. [CrossRef]
83. Roller, J.M.; Arellano-Jiménez, M.J.; Jain, R.; Yu, H.; Carter, C.B.; Maric, R. Oxygen Evolution during Water Electrolysis from Thin Films Using Bimetallic Oxides of Ir-Pt and Ir-Ru. *J. Electrochem. Soc.* **2013**, *160*, F716–F730. [CrossRef]
84. Siracusano, S.; Hodnik, N.; Jovanovic, P.; Ruiz-Zepeda, F.; Šala, M.; Baglio, V.; Aricò, A.S. New insights into the stability of a high performance nanostructured catalyst for sustainable water electrolysis. *Nano Energy* **2017**, *40*, 618–632. [CrossRef]
85. Thompson, K.; Larson, D.J.; Ulfig, R.M. Pre-sharpened and Flat-top Microtip Coupons: A Quantitative Comparison for Atom-Probe Analysis Studies. *Microsc. Microanal.* **2005**, *11*, 882–883. [CrossRef]
86. Schweinar, K.; Nicholls, R.L.R.L.; Rajamathi, C.R.C.R.; Zeller, P.; Amati, M.; Gregoratti, L.; Raabe, D.; Greiner, M.; Gault, B.; Kasian, O. Probing catalytic surfaces by correlative scanning photoemission electron microscopy and atom probe tomography. *J. Mater. Chem. A.* **2020**, *8*, 388–400. [CrossRef]